Obtaining Ising-like expansions for binary alloys from first principles

2002 Modelling Simul. Mater. Sci. Eng. 10 685

(http://iopscience.iop.org/0965-0393/10/6/306)

INSTITUTE OF PHYSICS PUBLISHING MODELLING AND SIMULATION IN MATERIALS SCIENCE AND ENGINEERING

Modelling Simul. Mater. Sci. Eng. **10** (2002) 685–706 PII: S0965-0393(02)40123-4

Obtaining Ising-like expansions for binary alloys from first principles

Alex Zunger[1], **L G Wang**[1], **Gus L W Hart**[2] **and Mahdi Sanati**[1]

[1] National Renewable Energy Laboratory, Golden, Colorado, CO 80401, USA
[2] Department of Physics and Astronomy, Northern Arizona University, Flagstaff, Arizona, AZ 86011-6010, USA

Received 10 March 2002, in final form 29 July 2002
Published 3 October 2002
Online at stacks.iop.org/MSMSE/10/685

Abstract

Many measurable properties of crystalline binary $A_{1-x}B_x$ alloys, such as phase diagrams and excess thermodynamic functions, could be predicted via lattice statistical mechanics methods if one knew the 'configurational energy'. The latter describes the energy at $T = 0$ for each of the 2^N possible occupation patterns of the N lattice sites by an A or a B atom. Traditional approaches described the configurational energy either via empirically fitted, truncated Ising Hamiltonians, or through highly approximated coherent-potential constructs. We illustrate here the alternative approach of 'mixed-basis cluster expansion' which extracts from a set of *ab initio* local density approximation calculations of the total energies of a few ordered A–B compounds a complete configurational energy function. This method includes both pair and multibody terms, whose number and range of interaction are decided by the variational procedure itself, as well as long-range strain terms. In this paper, we describe the computational details of this method, emphasizing methods of construction, interpolations, fits and convergence. This procedure is illustrated for Ni–Pt, Cu–Au and ScS–□S (where □ denotes cation vacancy). The parameters of the final expansions are provided on our webpage (http://www.sst.nrel.gov).

1. Introduction: representing the configurational energy of alloys

Many electronic and structural properties of $A_{1-x}B_x$ alloys can be predicted theoretically if one knows the 'configurational energy function' [1,2] $E_{\text{config}}[\{S_i\}; \{\boldsymbol{R}_i\}]$, providing the energy at $T = 0$ for each occupation pattern of the N lattice sites with the ith site occupied by either an A or B atom. Here, S_i denotes the pseudo-spin at the ith lattice site, taking the value -1 (+1) if it is occupied by A (B), and $\{\boldsymbol{R}_i\}$ are the position vectors of the atom. Given the configurational energy function for a particular A–B alloy system, one can, for example, search the $T = 0$ 'ground states', i.e. the stable crystal structures in that system [3–5]. Coupling $E_{\text{config}}[\{S_i\}, \{\boldsymbol{R}_i\}]$ to Monte-Carlo simulation provides the equilibrium phases at (x, T), and thus the phase diagram [6]; through thermodynamic integration [7], one can obtain the entropy

of the system. Finally, such simulations give directly the short-range-order parameters [8, 9] $\alpha(x, T)$ and mixing enthalpies [10, 11].

The configurational energy $E_{\text{config}}[\{S_i\}, \{\boldsymbol{R}_i\}]$ can be modelled at different levels of approximation. One distinguishes between 'direct approaches' and 'cluster expansions' (CE). In a direct approach, one minimizes the total energy for a given occupation pattern, with respect to local atomic displacements $\{\boldsymbol{R}_i\}$, yielding $E^{\text{eq}}_{\text{config}}[\{S_i\}]$. This can be done either quantum mechanically [12, 13], i.e. $E_{\text{QM}}(\sigma) = \langle\Psi|H|\Psi\rangle/\langle\Psi|\Psi\rangle$, or via interatomic potentials [14, 15] (e.g. the embedded atom method), $E_{\text{config}} = \sum_{ij} V_{ij} + \sum_{ijk} V_{ijk} + \cdots$. The direct *quantum mechanical* approach is limited to systems with a small number of atoms (per unit cell) and to a rather small number of different occupation patterns ('lattice configurations'), whereas the use of empirical *interatomic potentials* is not always reliable for arbitrary alloy systems. However, the direct approaches explicitly incorporate specific cohesive forces in the calculation of E_{config} (metallic bonding, electrostatics, exchange-correlation, etc); so it is possible to analyse *ex post facto* alloy thermodynamics in terms of these fundamental bonding mechanisms.

The alternative 'CE' approach [1, 2] to construct E_{config} is to expand E_{config} at the outset in terms of 'geometric objects' (GOs) such as points, pairs, triangles, and associate with each GO a characteristic energy J_{GO}. The most famous example of such a CE is the Ising-like expansion [6, 16] which describes the energy as

$$E_{\text{config}}(\sigma) = J_0 + J_1 \sum_i S_i(\sigma) + \sum_{j<i} J_{ij} S_i S_j + \sum_{k<j<i} J_{ijk} S_i S_j S_k + \cdots . \qquad (1)$$

Here, the configuration σ corresponds to a particular occupation pattern S_i ($i = 1, \ldots, N$). In this approach, E_{config} corresponds to the fully relaxed positions $\{R_i\}$ of the basis atoms in the cell so that the J_{GO} correspond to cluster interactions of the atomically relaxed system. Thus, although the relaxed positions (i.e. the local displacements of the basis atoms away from the ideal lattice sites) are not given explicitly, they are fully included in the CE implicitly. The format of equation (1) lends itself to convenient searching of the configurational space [3]. Furthermore, since in its truncated form $E_{\text{config}}(\sigma)$ can be calculated essentially effortlessly for each σ, coupling to statistical mechanics simulations (Monte-Carlo, Cluster Variation Method) is computationally feasible [6, 16].

For some time, the prevailing culture in 'CE' approaches [6, 16–19] for constructing E_{config} was to treat $\{J_{\text{GO}}\}$ as adjustable parameters and fit to the observed properties of the alloy. Thus one would truncate equation (1) to include an arbitrarily small number of terms (the classic Ising model retains just the first neighbour term J_{NN}) and fix the value of J by fitting the order–disorder transition temperature [18] $T_{\text{c}} = \alpha J_{NN}$, or the formation enthalpy [19] of an ordered A–B phase $\Delta H_{AB} = \beta J_{NN}$, where α and β are numerical constants, or one would fix certain ratios J_{NN}/J_{NNN} between first and second nearest neighbour to reproduce a given ground state structure [3]. This approach has thus transformed many questions in the field of alloy phase stability into the quest for a set of parameters $\{J\}$ that reproduce measured alloy behaviour. However, this approach, by itself, does not determine what is the physical range of the pair interactions in equation (1), or the type of geometric objects (pair, three body, four body, etc) that pertain to a given alloy system, or the physical origin of the relevant cohesive forces (elastic, charge transfer, electrostatic, etc). Also, fitting to transition temperatures [20] or fitting to short-range-order parameters [21] produces J's that fail to reproduce correct formation energies. Indeed, because these approaches provide, as just stated, a parametrization for only a narrow range of properties, they often fail to correctly model unknown regions in the phase diagram or accurately predict ground state structures for the full range of composition.

What one needs is an electronic structure theory which *independently* establishes, for a given $A_{1-x}B_x$ system, the range, type, physical origin and magnitude of the interaction energies $\{J\}$. Early attempts at this goal include the 'generalized perturbation method' [4]

and the 'concentration wave method' [22], which involve various approximations beyond the first-principles local density approximation (LDA) that underlies these approaches. In their various forms, these methods ignored atomic relaxation of even size-mismatched systems, approximated the total energy just by the sum of energy eigenvalues, and until recently [23], overlooked the Madelung contribution to the energy of ionic alloys. Here we will discuss how a robust CE can be obtained directly from LDA calculations on a few ordered A_pB_q structures. This 'mixed-basis cluster-expansion' (MBCE) approach [1, 24] builds on and extends the Connolly–Williams [25] approach. We have recently applied this method to predict thermodynamic behaviour of numerous binary alloys, including Cu–Au [26–28], Cu–Ag [26], Cu–Pt [29, 30], Ni–Au [26, 28, 31], Ag–Au [32, 33], Cu–Pd [33], Ni–V [34, 35], Ni–Pt [36], Ag–Pd [37, 38], Al–Zn [10, 39], Pd–V [34, 35], Pd–Pt [32], Cu–Al [10] and Cu–Zn [40] and some semiconductor alloys [20, 41, 42]. Such CEs are then used in Monte-Carlo simulations of the Hamiltonian. This yields phase diagrams, ground state structures, thermodynamic functions, short-range-order profiles and precipitate shapes.

In this paper, we illustrate in detail how such an expansion is constructed from LDA total energies. We focus on the technical issues of how a robust fit is achieved, how structures are chosen and how a stable expansion is obtained. We illustrate this using three systems: Ni–Pt, Cu–Au and $Sc_{1-x}\,\square_x$ S (where $\square$ denotes a vacancy on the Sc site)[3]. We chose Ni–Pt and Cu–Au because they are paradigm binary alloys. We will show that with our MBCE method, we can predict ground state structures that are not yet known or even suspected. The example of $Sc_{1-x}\,\square_x$S shows that the CE methodology can also be applied to vacancy-ordering compounds and not just to 'proper' alloys. Although we specifically discuss alloys based on cubic sublattices, generalization to cases of other crystal symmetries should be straightforward.

2. The structure of the MBCE

In the MBCE, any configuration σ is defined by specifying the occupation of each of the N lattice sites by an A atom (spin index $S_i = -1$) or a B atom ($S_i = +1$). The formation enthalpy of any configuration σ is conveniently given by

$$\Delta H_{\mathrm{CE}}(\sigma) = E_{\mathrm{pair}}(\sigma) + E_{\mathrm{multibody}}(\sigma) + E_{\mathrm{CS}}(\sigma). \tag{2}$$

The first term $E_{\mathrm{pair}}(\sigma)$ includes all pair figures, where $J_{\mathrm{pair}}(\boldsymbol{k})$ and $S(\boldsymbol{k}, \sigma)$ are lattice Fourier transforms of real-space pair interactions and spin-occupation variables:

$$E_{\mathrm{pair}}(\sigma) = \sum_{\boldsymbol{k}} J_{\mathrm{pair}}(\boldsymbol{k})|S(\boldsymbol{k}, \sigma)|^2. \tag{3}$$

The second term $E_{\mathrm{multibody}}(\sigma)$ includes multibody interactions and runs over symmetry-inequivalent clusters, such as empty, single, three, four and more lattice site clusters:

$$E_{\mathrm{multibody}}(\sigma) = \sum_{f}^{\mathrm{MB}} D_f J_f \bar{\Pi}_f(\sigma). \tag{4}$$

Here, D_f is the number of equivalent clusters per lattice site and $\bar{\Pi}_f(\sigma)$ are structure-dependent geometrical coefficients [20] (spin products). These first two terms of equation (2) include all the information about the strength and importance of the different chemical interactions characterized by effective cluster interactions J_{pair} and J_f. However, the strain energy (due by the lattice mismatch) necessary to maintain coherency at an interface between regions of

[3] Because ScS-$\square$S is a *pseudo*-binary system (the S atom is just a spectator), the same binary formalism can used for this system. Specifically, $S_i = +1$ for a Sc atom and $S_i = -1$ for a Sc vacancy, $\square$.

pure A and B cannot be expressed by these finite-ranged Js. Consequently, this contribution, $E_{\rm CS}(\sigma)$, to the formation enthalpy is expressed by the last term in equation (2):

$$E_{\rm CS}(\sigma) = \sum_{\boldsymbol{k}} \frac{\Delta E^{\rm eq}_{\rm CS}(x,\hat{k})}{4x(1-x)} |S(\boldsymbol{k},\sigma)|^2 F(\boldsymbol{k}), \tag{5}$$

where $\Delta E^{\rm eq}_{\rm CS}(x,\hat{k})$ is the *constituent strain energy* [8,24], which is defined as the strain energy required to maintain coherency along an interface (with orientation $\hat{k}$) of bulk A and B.

To understand the necessity for this term in the CE, consider coherent phase separation, i.e. solid A and B coherently match along the crystallographic direction $\hat{k}$ (formally, this is a long-period superlattice A_n/B_n with $n \to \infty$ oriented along $\hat{k}$). These long-period structures possess small ($\boldsymbol{k} \to 0$) dominant wavevectors in $S(\boldsymbol{k},\sigma)$, but their strain energy depends on the layer orientation, and thus the direction of $\boldsymbol{k}$. However, the CE of equation (2) *without* $\Delta E_{\rm CS}$ and with the finite-ranged interactions $J_{\rm pair}$ and $J_{\rm multibody}$ will give [24] for superlattices, $\Delta H(n) \sim 1/n$ as $n \to \infty$, *independent* of $\hat{k}$. But in reality, the energy of A_n/B_n with $n \to \infty$ is a finite quantity (the energy of strained A plus strained B) which, moreover, depends on $\hat{k}$ [43]. Thus, one must include a $\Delta E_{\rm CS}$ term in equation (2) since this introduces the orientation dependence in the energy of the coherently strained two-phase system which cannot be described by finite-ranged real-space interactions $J(R)$. Further, because long-period superlattices possess $\boldsymbol{k} \to 0$ dominant wavevectors but the strain energy is dependent on the direction of $\hat{k}$, there is a $\boldsymbol{k} \to 0$ non-analyticity in the reciprocal-space description of the coherency strain.

In other words, the value of the constituent strain in the limit as $k \to 0$ depends on the *direction* in which the limit is taken. Our formulation of $\Delta E_{\rm CS}$ treats this direction dependence correctly and retains the correct $n \to \infty$ superlattice limit. This form gives the correct orientation and composition dependence in the long-period limit of the coherency strain. Furthermore, it was shown that this form is also uniquely defined for short-period superlattices and non-superlattices. The attenuation function $F(\boldsymbol{k})$ is taken as $\exp(-|\boldsymbol{k}|/|\boldsymbol{k}_{\rm c}|)^2$ and permits one to treat short-period superlattices ($k \to 2\pi/n$) differently than long-period superlattices ($k \to 0$).

For each configuration σ, the quantities $\bar{\Pi}_f(\sigma)$, D_f and $S(\boldsymbol{k},\sigma)$ are determined geometrically. Given these three quantities, as well as the $\Delta E^{\rm eq}_{\rm CS}(x,\hat{k})$ obtained from LDA calculations for the end point elements, pure A and B solids, the unknowns in equations (3)–(5) are $\{J_{\rm pair}(\boldsymbol{k})\}$ and $\{J_f\}$. These are obtained by fitting a set of directly calculated LDA formation enthalpies of some ordered configurations σ_s to the CE expression of equation (2). The formation enthalpy of an ordered A_pB_q bulk compound is defined as the energy gain or loss with respect to the bulk constituents at their equilibrium lattice constants:

$$\Delta H_{\rm LDA}(\sigma) = E^{\rm tot}(A_pB_q,\sigma) - (1-x)E^{\rm tot}_A(a_A) - xE^{\rm tot}_B(a_B). \tag{6}$$

Here, a_A and a_B are equilibrium lattice constants of the bulk solids A and B, and $E^{\rm tot}_A(a_A)$ and $E^{\rm tot}_B(a_B)$ are the total energies of A and B, respectively; whereas $x(=q/(p+q))$ is the concentration of B in the ordered configuration σ. As shown earlier (see, e.g. [1]), it is essential that the calculated energies $E^{\rm tot}(A_pB_q,\sigma)$ correspond to the *geometrically fully relaxed configuration*, i.e. the structures have to be optimized (conserving the symmetry of the structure) with respect to unit cell vectors, cell-internal atomic displacements and the volume of the unit cell. In what follows, we describe in detail how the CE of equation (2) is determined in practice. This is going to establish a first-principles Ising-like expansion where the range, type, physical origin and magnitude of the interactions are determined via a microscopic model of cohesion.

3. Determination of the expansion coefficients in the MBCE

3.1. The constituent strain

Determining $\Delta E^{\rm eq}_{\rm CS}(x,\hat{k})$ requires three steps: (i) calculating the epitaxial energies of each end point, A and B for several directions $\hat{k}$ and in-plane lattice constant $a_\perp$, (ii) finding the $a_\perp$ that minimizes the total $A + B$ epitaxial energies for intermediate concentrations and (iii) interpolating the results of (ii) to arbitrary directions of $\hat{k}$.

For the first step, one calculates via LDA for pure A and pure B the total energy of several different in-plane lattice constants, $a_\perp$ (perpendicular to $\hat{k}$), and in each case, the unit cell is allowed to relax in the direction perpendicular to the interface to minimize the total energy. This series of energies, $E^{\rm epi}_{A,B}(\hat{k},a_\perp)$, is then interpolated to all in-plane lattice constants $a_\perp$ between a_A and a_B using a polynomial. This process is repeated for five principal directions of $\hat{k}$—(001), (011), (111), (201) and (311). The results are illustrated in figure 1 for Ni and Pt.

In the second step, $E^{\rm eq}_{\rm CS}(x,\hat{k})$ is determined from the total epitaxial energy of $E^{\rm epi}_A(\hat{k},a_\perp)$ and $E^{\rm epi}_B(\hat{k},a_\perp)$. That is,

$$\Delta E^{\rm eq}_{\rm CS}(x,\hat{k}) = \min_{a_\perp}[(1-x)\Delta E^{\rm epi}_A(\hat{k},a_\perp) + x\Delta E^{\rm epi}_B(\hat{k},a_\perp)], \tag{7}$$

where the equilibrium in-plane lattice constant $a_\perp$, common to both A and B, is chosen to minimize the strain energy, and $\Delta E^{\rm epi}(\hat{k},a_\perp) = E^{\rm epi}(\hat{k},a_\perp) - E^{\rm epi}(\hat{k},a_{eq})$. The constituent strain energy $E^{\rm eq}_{\rm CS}(x,\hat{k})$ is determined for arbitrary compositions x and a finite number of directions $\hat{k}$. The lattice constant which minimizes equation (7) for each $(x,\hat{k})$ is shown in figure 2 for Ni–Pt and Cu–Au. Figure 3 shows the constituent strain energy of equation (7) for

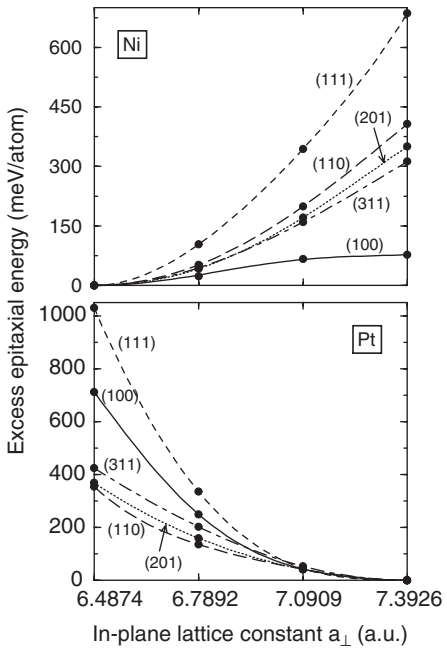

Figure 1. Excess epitaxial energy $\Delta E^{\rm epi}(\hat{k},a_\perp) = E^{\rm epi}(\hat{k},a_\perp) - E^{\rm epi}(\hat{k},a_{\rm eq})$ of Ni and Pt plotted vs in-plane lattice constant $a_\perp$ for five directions $\hat{k}$.

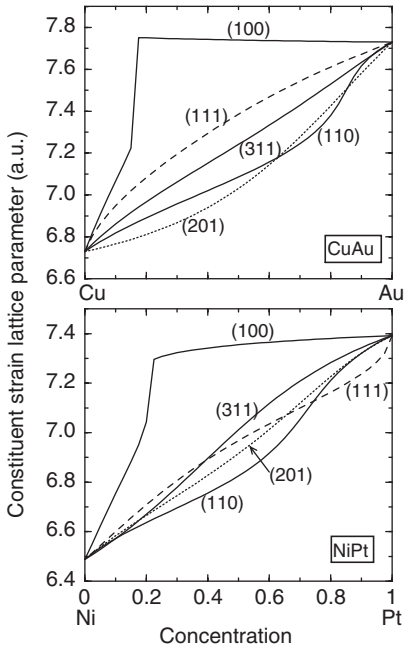

Figure 2. Equilibrium lattice parameter which minimizes $\Delta E_{\mathrm{CS}}^{\mathrm{eq}}(x, \hat{k})$ of equation (7) for Ni–Pt and Cu–Au for five directions $\hat{k}$.

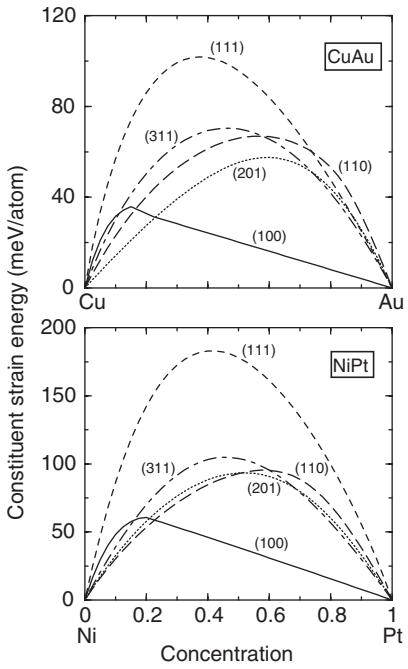

Figure 3. Equilibrium constituent strain energies $\Delta E_{\mathrm{CS}}^{\mathrm{eq}}(x, \hat{k})$ vs x (equation (7)) for Ni–Pt and Cu–Au for five directions $\hat{k}$.

five principal directions. Naturally, each of the energies $\Delta E_A^{\rm epi}$ and $\Delta E_B^{\rm epi}$ is positive definite and, hence, the coherency strain of equation (7) must be positive definite.

Finally, in the third step, the constituent strain energy is interpolated to arbitrary directions of $\hat{k}$ by fitting the results to an expansion of Kubic harmonics. That is, after $E_{\rm CS}^{\rm eq}(x,\hat{k})$ has been directly calculated for a set of directions using total energy methods, it is then interpolated to all directions by fitting the directly calculated results the following expression:

$$\Delta E_{\rm CS}^{\rm eq}(x,\hat{k}) = \sum_{l=0}^{l_{\rm max}} b_l(a_\perp) K_l(\hat{k}). \tag{8}$$

In cubic alloys, only terms with $l = 0, 4, 6, 8, 10, 12, \ldots$ are non-zero and only these enter into the expansion. If only the first two terms are retained, then (8) reduces to well-known expression from harmonic elasticity theory (see discussion in [44]). However, our experience shows that anharmonic effects are usually significant, and so, in practice, we normally fit the data using at least four terms in equation (8), i.e. $l_{\rm max} = 8$. Figure 4 depicts $E_{\rm CS}^{\rm eq}(x,\hat{k})$ for Ni–Pt and Cu–Au as a parametric plot in all directions.

In summary, $\Delta E_{\rm CS}^{\rm eq}(x,\hat{k})$ is determined as follows:

(a) Epitaxial calculations are performed for each constituent of the alloy, A and B. For a series of different in-plane lattice constants $a_\perp$ ($a_A \leqslant a_\perp \leqslant a_B$), the total energy is minimized by varying the out-of-plane lattice constant (parallel to $\hat{k}$) while the in-plane lattice constant

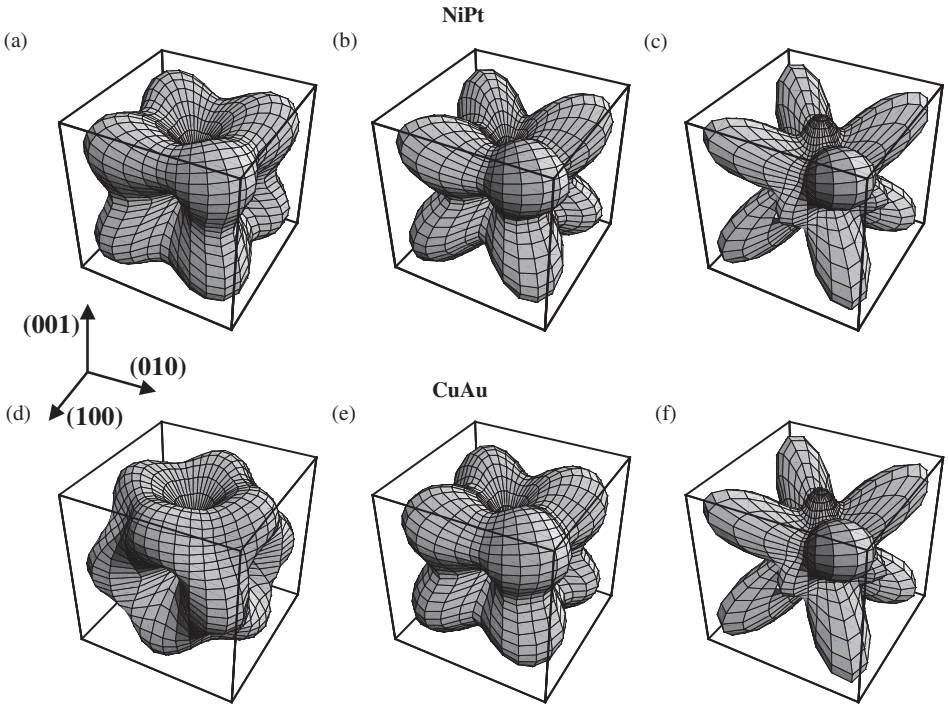

Figure 4. Parametric three-dimensional presentation of the constituent strain energies $\Delta E_{\rm CS}^{\rm eq}(x,\hat{k})$ of equation (8) for Ni–Pt and Cu–Au. (*a*) 10% Ni; (*b*) 50% Ni; (*c*) 90% Ni; (*d*) 10% Cu; (*e*) 50% Cu; and (*f*) 90% Cu. The [111] direction is the hardest for Ni–Pt. For Cu–Au the [110] direction is the hardest for Au-rich alloys ($\geqslant$75% Au), and the [111] direction is the hardest for alloys with less than 75% Au.

is held fixed. These values, $E_{\rm epi}(a_\perp)$, are interpolated to all values between a_A and a_B by a polynomial fit.

(b) The strain energy for any composition x is taken to be the weighted average of the epitaxial energies calculated in (a) but we choose the in-plane lattice constant $a_\perp$ to minimize the strain energy as shown in equation (7).

(c) The strain energy for several directions $\hat{k}$ is determined by repeating (a) and (b) for each direction $\hat{k}$. In practice, we use 5–7 different $\hat{k}$-directions. These directly calculated $\hat{k}$-dependent values for the strain energy are then interpolated to arbitrary values of $\hat{k}$ by fitting to an expansion in Kubic harmonics, as shown in equation (8). Because of anharmonic effects, we typically find it necessary to use at least four terms in equation (8).

3.2. The constrained CE fit

In constructing the fit of $\Delta H_{\rm CE}(\sigma)$ to $\Delta H_{\rm LDA}(\sigma)$, it is advantageous to use a different number interaction energies J than the number of LDA-calculated input formation enthalpies. This is unlike the Connolly–Williams approach [25] where the number of input structures and interaction energies must be the same, so a large number of LDA calculations might be needed to obtain a converged expression. However, at the same time, we must avoid 'over-fitting' by using too many interaction energies which results in a very accurate *fit* but a very poor *prediction* for structures not included in the fit. To achieve these objectives, we can require that $J_{\rm pair}(\boldsymbol{k})$ be a smooth function of $\boldsymbol{k}$. We define [24] a 'smoothness value' M as

$$M = \frac{1}{\alpha} \sum_{\boldsymbol{k}} J(\boldsymbol{k}) \left[-\nabla_{\boldsymbol{k}}^2\right]^{\lambda/2} J(\boldsymbol{k}), \tag{9}$$

where the exponent λ is a free parameter. Minimizing the value M guarantees both the smoothness of the pairs in k-space and that the magnitude of the pair interactions generally decreases with distance.

Our fitting procedure will be to minimize the quantity

$$\sum_{\sigma \in s} w_\sigma |\Delta H_{\rm LDA}(\sigma) - \Delta H_{\rm CE}(\sigma)|^2 + tM \tag{10}$$

by varying $\{J_f\}$ (for the non-pair figures included in the expansion) and $J_{\rm pair}$ (for the pair figures). Here $\Delta H_{\rm LDA}$ is the directly calculated energy (equation (6)), $\Delta H_{\rm CE}$ is defined in equation (2) and t is a Lagrange scaling factor. Note that using $t = 0$ is equivalent to eliminating the smoothness condition and results in a standard real-space fit. In this case, the long-range interactions may be as strong as (or even stronger than) the short-range interactions, a clearly unphysical situation which can reduce the *predictive* accuracy of the CE. By subjecting the pair interactions to the smoothness criterion as shown in equation (10), a more physically sensible, more predictive set of interactions is obtained, and over-fitting is avoided[4].

4. The computational procedure

4.1. Selection of structures for LDA calculations

In selecting the structures for input set, we begin with typical structures of binary compounds ('the usual suspects') as well as a set of A_pB_q superlattices along the principal directions (001), (110), (111), (201) and (311) which span the full range of compositions. Table I in

[4] In practice, the smoothness criterion is imposed in a real-space fitting procedure that is formally equivalent to the k-space expressions presented here. See section VB of [24].

[40] and table III in [28] give a typical list of input structures. These structures need not be lowest-energy structures. We use four criteria to establish additional structures to add to the input set.

(i) We use the method of Ferreira *et al* [20] to determine whether a proposed structure exhibits approximately linear dependence of its $\bar{\Pi}$ with that of the structures already included in the input set. We wish to avoid including structures that are nearly linearly dependent because this leads to instability in the fitting procedure. Selecting linearly independent structures is also more efficient as each structure brings 'new information' to the fit, thus reducing the number of structures that need to be included and consequently reducing the total number of LDA calculations that must be performed.

(ii) We often add to our list of structures a few of supercell models of the random alloy using the 'special quasirandom structures' (SQSs) approach [45]. This assures that the CE can model not only ordered, but also disordered phases accurately.

(iii) Once we have a tentative MBCE, we calculate the 'ground state structures' [5] produced by this expansion, scanning all possible unit cells with $N_{\max}$ (or less) atoms/cell (usually, $N_{\max} \leqslant 20$; see section 4.3 below). The ground state structures are determined by constructing a 'convex hull'. The convex hull is a set of straight line segments that connect the set of configurations (including the pure element end points) that are stable with respect to separation into (any) other structures of neighbouring concentrations. The structures connected by the line segments of the convex hull, also called 'breaking points', are the ground states of the alloy system because they are globally stable. If the convex hull of the tentative MBCE predicts new ground states not in the input set, the LDA energy of these structures is calculated and they are added to the input set and a new MBCE is computed. This 'direct enumeration' approach to constructing the ground state hull is more exhaustive than the typical Monte Carlo based simulated annealing approach used in many previous studies, although it is subject to the (very reasonable) limitation that the search only considers candidate structures of $\leqslant$20 atoms/cell.

(iv) No *finite* CE can predict exactly the energy of all configurations. Forcing the MBCE to accurately fit or predict configurations with energy much higher than the ground states can drastically slow down the convergence of the MBCE [46]. Such 'high-energy' structures are not physically relevant and consequently, we introduce a cut-off energy E_{cut}, so any of the structures whose energy is found to lie above the convex hull by an amount $\geqslant E_{\text{cut}}$ is excluded from the input set.

If a given structure satisfies conditions (i)–(iv) and is to be included in the fit, we calculate its LDA formation enthalpy following equation (6). Particular care is exercised to maintain comparable precision in both the energy $E^{\text{tot}}(A_pB_q)$ of the compound and that of the end points, E_A^{tot} and E_B^{tot}. This is done by using a set of k-points for the compound that is *equivalent* [47] to that used for the calculations of the end points. Choosing a single equivalent k-point mesh that is commensurate for all compounds is not always possible. For fcc-based alloys, we normally choose a k-mesh equivalent to the 60 special points of the $8 \times 8 \times 8$ mesh, when the unit cell vectors of the ordered compound permit. For structures that are incommensurate with the $8 \times 8 \times 8$ fcc mesh, we calculate the total energies of the compound and end-point constituents with a finer k-point grid. The procedure of equivalent k-points ensures that, due to systematic cancellation of errors, the formation enthalpies converge (with respect to the fineness of the k-point mesh) much faster than the total energies of the compound and the end-point elements. Also, attention is paid to obtaining equivalent precision in the calculated energies of A, B and A_pB_q in terms of FFT and other integration grids.

4.2. Selection of the type of cluster interactions

The interaction energies J are determined by minimizing equation (10). Of course an excellent fit can be obtained by using a large number of fitting parameters but such 'over-fitting' destroys the predictive accuracy of the CE. We desire a CE which accurately fits the input structures *and* accurately predicts the formation enthalpy of structures *not* included in the fit. In practice, we accomplish this by dividing the N_s members of the LDA input set into two groups. The first group of N_f structures is those 'included in the fit', i.e. they are used to produce the interaction energies. In contrast, the second group of N_p structures are reserved for predictions. We monitor the fitting error,

$$R_{\rm fit} = \sqrt{\frac{\sum_{\sigma=1}^{N_f}(\Delta H_{\rm LDA}(\sigma) - \Delta H_{\rm CE}(\sigma))^2}{N_f}}, \tag{11}$$

and prediction error,

$$R_{\rm pred} = \sqrt{\frac{\sum_{\sigma=N_f+1}^{N_s}(\Delta H_{\rm LDA}(\sigma) - \Delta H_{\rm pred}(\sigma))^2}{N_p}}. \tag{12}$$

The ideal cluster expansion will find the best compromise to simultaneously minimizing both of these quantities for any set of 'fitted' and 'predicted' structures. Thus, the number of pairs ($N_{\rm pair}$), the smoothness parameters (t and λ) and the choice of multibody terms should be chosen to optimize $R_{\rm fit}$ and $R_{\rm pred}$ for different choices of these parameters. Our (heuristic) method for performing this optimization is as follows:

(i) the number of pair interactions $N_{\rm pair}$ is varied while λ, t (equations (9) and (10)), and the $N_{\rm MB}$ (equation (4)) are held fixed;
(ii) a range of λ values is scanned while $N_{\rm pair}$, t and $N_{\rm MB}$ are held fixed;
(iii) a range of t values is scanned while λ, $N_{\rm pair}$ and $N_{\rm MB}$ are held fixed;
(iv) the number of multibody terms $N_{\rm MB}$ is varied while λ, t and $N_{\rm pair}$ are held fixed.

After optimizing the CE by completing steps (i)–(iv) above, we subject it to two tests. First, we identify sensitive structures by calculating the 'elimination error', i.e. we use $N_s - 1$ structures for the fit, and predict the error in the energy of the eliminated structure. This is repeated for all N_s structures. This test identifies which structure is a sensitive structure. The structures with large 'elimination errors' have to be included in the fit, otherwise the fit error increases significantly. The second test is loosely referred to as a 'ground state consistency' test. At each concentration, we check to see that the input structures computed by LDA retain their energy ordering (with respect to each other) when predicted by the MBCE. Additionally, we check to see whether the convex hull constructed using the LDA-calculated values of the input structure matches that constructed using the MBCE-fitted/predicted values.

4.3. Iterating the fit

The fit is done iteratively. In each iteration we might change $\{\lambda, t, N_{\rm pair}, N_{\rm MB}\}$, add structures (e.g. new ground states) and/or eliminate structures (e.g. structures with energies far above the ground state hull). If the $R_{\rm fit}$ value is too large, then one must increase the number of pair and multibody interactions. This may lead to 'over-fitting' ($R_{\rm pred}$ will become too large) or poor performance of the CE during the 'ground state consistency' test. When this happens, more input structures must be included in the input database (i.e. more LDA calculations are necessary).

Once we have a set $\{\lambda, t, N_{\rm pair}, N_{\rm MB}\}$ that has minimal errors in $R_{\rm fit}$ and $R_{\rm pred}$, passes the 'ground-state consistency test', and accurately treats the structures identified as having high

'elimination errors', we use this expansion to calculate the ground states. We use the 'direct enumeration' procedure of Ferreira *et al* [5]. Any new ground state that is predicted by this search is added to the list of input structures and steps (i)–(iv) of section 4.2 are then repeated. The following section uses three different examples to illustrate this procedure.

5. Illustrating the procedure

We illustrate the procedures of section 4 using Ni–Pt, Cu–Au and $Sc_{1-x}\,\square_x S$ as examples. The LDA calculations for Ni–Pt and $Sc_{1-x}\,\square_x S$ were done using pseudo-potential plane-wave method. The constituent strain term is included for Ni–Pt and Cu–Au, but not for $Sc_{1-x}\,\square_x S$, because the constituent strain energy for this case is not positive definite (because the $x = 1$ end-point material, $\square S$ (essentially fcc sulfur), is not stable).

Figure 5 illustrates for Ni–Pt how the fitting (upper panels) and prediction (lower panels) errors are affected by different values of t, λ and N_{pair}. We have used for Ni–Pt a set of $N_{\text{f}} = 32$ structures for the fit, plus $N_{\text{p}} = 3$ structures for predictions. The fit and prediction errors depend on the structures chosen. Naturally, as the number of pair interactions increases (figure 5(a)), the *fitting* error decreases monotonically. However, the *prediction* error goes through a minimum around $N_{\text{pair}} \sim 23$ (figure 5(b)), above which the system is 'over-fitted' with too many fitting parameters. Stopping at $N_{\text{pair}} = 23$, we optimize λ of equation (9) and t of equation (10) in figures 5(c)–(f), respectively. We see from figure 5(c) that as t increases, the quantity tM in equation (10) increases too, so the fit error must increase. But the prediction error (figure 5(d)) again goes through a minimum at some t ($t_{\text{min}} = 15$ for Ni–Pt, see the arrow in figure 5(d)). Note in figure 5(d) that using $t = 0$, which is equivalent to a real-space CE [25, 48, 49], one has a very large prediction error. Similarly, as λ increases the fit error decreases, but the prediction error goes through a minimum around $\lambda \sim 7$ (see the arrow in figure 5(f)). Figure 6 shows similar results for Cu–Au. We see that system has a minimum prediction error at $N_{\text{pair}} \sim 26$. Therefore, we choose $N_{\text{pair}} = 26$ and optimize λ and t as depicted in figures 6(c)–(f), respectively. In a similar procedure as mentioned above we find out that for Cu–Au system $\lambda \sim 2$ and $t \sim 20$ minimize our fitting and prediction errors. Figure 7 shows the results for ScS–$\square$S. For this system, we choose $N_{\text{pair}} = 25$, $t = 20$ and $\lambda = 2$. Figure 8 shows the elimination error test for Ni–Pt and Cu–Au. We plot the 'elimination error' for two iterations in the CE procedure: an early iteration, showing large elimination errors (dashed lines), and a well-optimized expansion, showing smaller elimination errors. In both cases, we identify some structures whose elimination from the fit does not cause any increase in error (e.g. L_{12a}, L_{12b} and DO_{22b} for Ni–Pt) and some 'sensitive structures' that must belong to the input set, or else the fit error increases significantly (e.g. W_2 for Ni–Pt and L_{10} and W_2 for Cu–Au). We emphasize that our final fit includes *all* of the $N_{\text{f}} + N_{\text{p}}$ structures (none eliminated), so the errors shown in figure 8 are larger than the actual errors in the final fit.

Figure 9 shows for Ni–Pt, Cu–Au and ScS–$\square$S the 'ground state consistency test' comparing the input LDA energies (circles) and fitted/predicted CE energies (crosses). We see that the fit is good, i.e. the crosses match the circles. In particular, the structures that are on the convex hull in LDA among the input structures are still on the same line in the CE fit.

Figures 10–12 show the calculated ground states of Ni–Pt, Cu–Au and ScS–$\square$S using the direct enumeration method for unit cells with up to 20 sites. The number of unique structures is 3 039 674 whereas for unit cells with 8 and 12 sites the number of structures is 670 and 12 098, respectively. We see that for Ni–Pt, we identify one unsuspected ground state structure at composition 12.5% Ni that was not initially part of the 'input set'. The

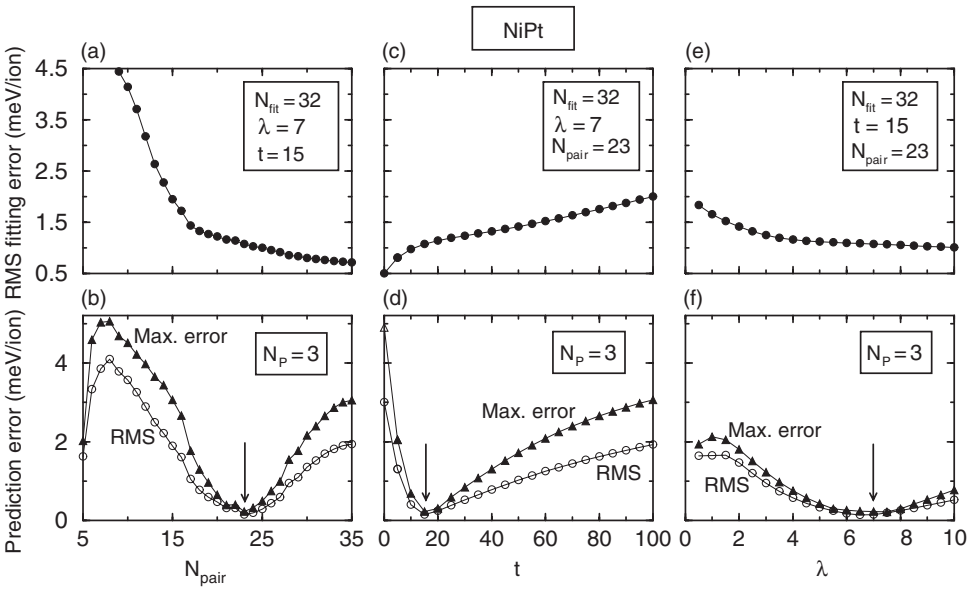

Figure 5. Fitting error (equation (11)) and the prediction error (equation (12)) as a function of the number of pair interactions N_{pair} in equation (3), the Lagrange multiplier t in equation (10) and the smoothness exponent λ in equation (9). The arrows point to the values used in the CE. Here N_{p} is the number of structures for prediction.

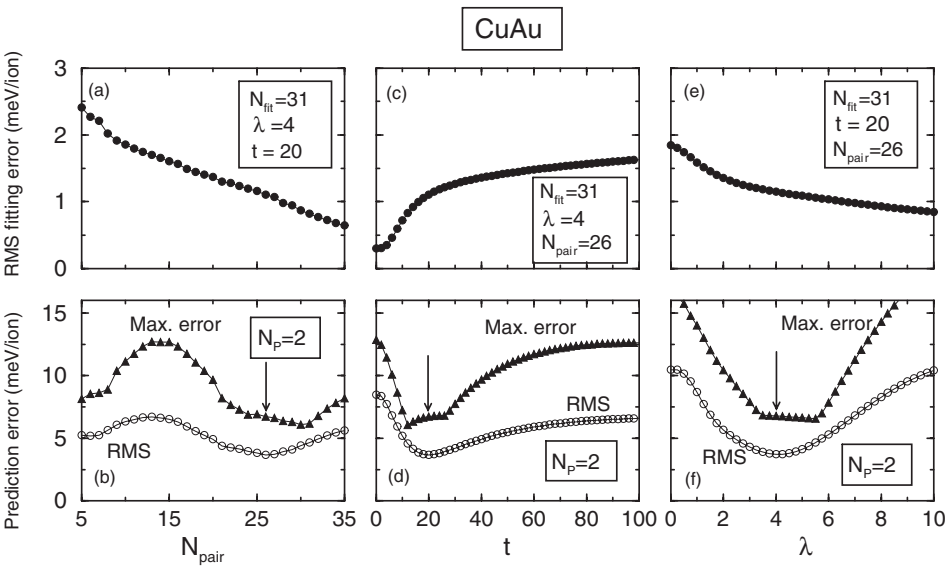

Figure 6. Fitting and prediction errors for Cu–Au as a function of N_{pair}, t and λ (see caption of figure 5).

atomic positions and unit cell vectors of this $NiPt_7$ structure were given in table 1. The crystal structure is shown in figure 13. Having identified this new ground state, we next calculated its LDA energy, finding ΔH_{LDA} ($NiPt_7$) $= -41.6$ meV atom^{-1}, compared with the CE prediction ΔH_{CE} ($NiPt_7$) $= -40.8$ meV atom^{-1}.

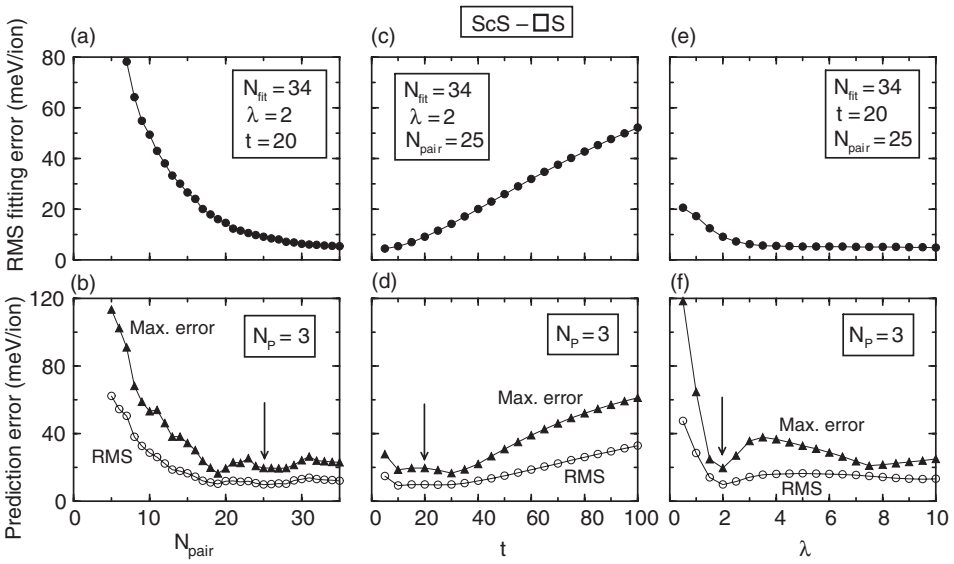

Figure 7. Fitting and prediction errors for ScS–□S as a function of $N_{\rm pair}$, t and λ (see caption of figure 5).

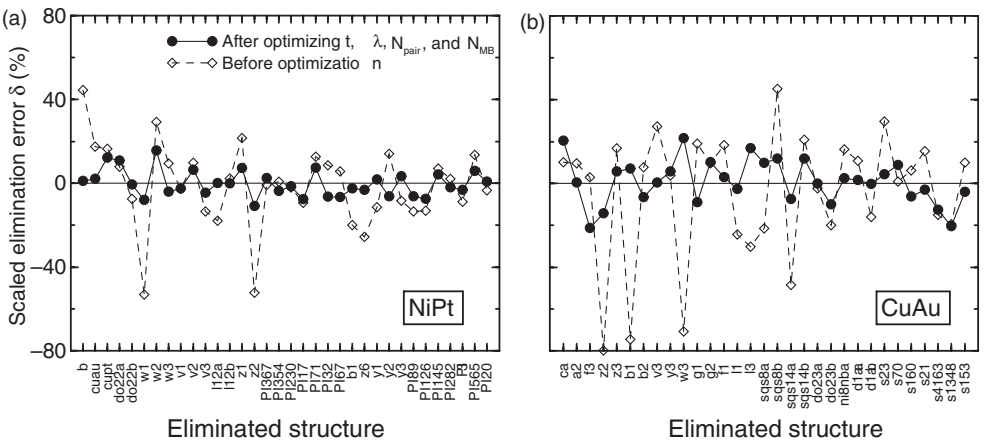

Figure 8. Elimination error test for Ni–Pt and Cu–Au. The 'scaled elimination error' is defined as: $\delta = ((\Delta H_{\rm pred}(\sigma) - \Delta H_{\rm LDA}(\sigma))/\Delta H_{\rm LDA}^{\rm avg}) \times 100\%$, where $\Delta H_{\rm LDA}^{\rm avg}$ is the average LDA formation enthalpy of $N_{\rm s}$ input structures, and $\Delta H_{\rm pred}(\sigma)$ is the formation enthalpy predicted by the CE for the structure which is not included in the fit. Here, δ is the CE prediction error of a given structure, eliminated from the input basis set used to perform the fit. Dashed lines: elimination error for an early CE iteration; solid lines: elimination error for a converged CE.

Next, we enquire if this structure is stable against separation into any other two structures at neighbouring concentrations. In other words, does it lie on or above the convex hull? We thus consider the two structures that in the *global* ground state search of figure 10 are neighbouring vertices to $NiPt_7$. This gives pure Pt at $x = 0$ and Pt_3Ni at $x = 25\%$ (figure 10). Their LDA energies $\Delta H_{\rm LDA}$ are 0 meV atom^{-1} and -65.1 meV atom^{-1}, respectively. We can now check if $NiPt_7$ is below the 'tie-line' connecting the two neighbouring ground states. We find that it lies 9.1 meV atom^{-1} below this tie line. Thus, $NiPt_7$ is stable against separation into its

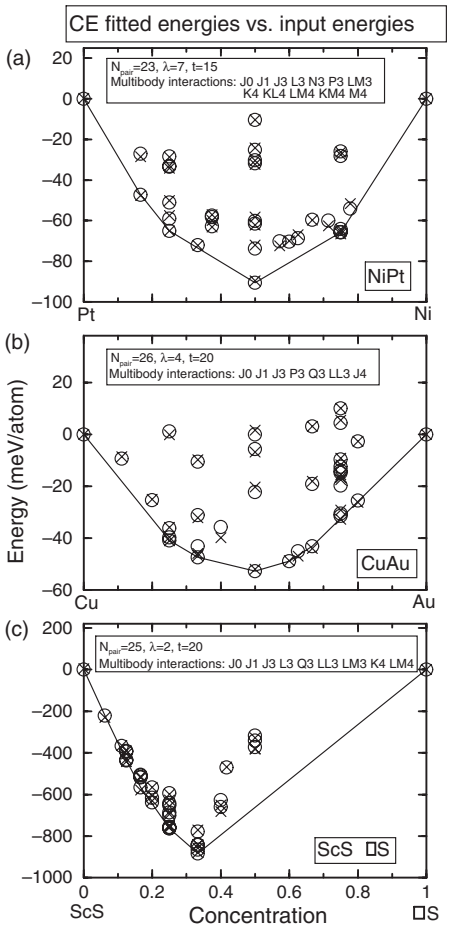

Figure 9. Ground state consistency test for Ni–Pt, Cu–Au and Sc_{1-x}–$\square_x$S. Crosses denote energies from the CE whereas circles denote input LDA energies. The solid line represents the convex hull of this set of configurations only. Note that within this set, the CE and LDA produce the same ground state structures.

neighbouring ground state structures not only in the CE, but also in LDA. Having verified that the new structure is a ground state, we add it to the 'input set' and repeat the optimization of λ, t, N_{pair} and N_{MB}. We find that to include the new ground state in the input set does not change the optimized values of λ, t, N_{pair} and N_{MB}. The ground states found in the ground state search are same as before without including this new ground state in the input set. This test shows that the present CE is converged.

Figure 11 describes the ground state search for Cu–Au for primitive unit cells containing up to 20 sites. The ground state searches for unit cells up to 8, 12 and 20 sites predict the same ground states. We see in figure 11 that there are two new ground states which are not part of the initial input set. The crystal structures, the atomic positions and unit cell vectors of three new ground states are shown in figure 14 and table 2, respectively. The set of ground states we find is larger than the set of ground states found in previous studies (see [26–28]). This is a result of using the direct enumeration approach instead of simulated annealing for the search of the ground states. An in-depth discussion of new ground states in the Cu–Au and Ni–Pt systems can be found in [50].

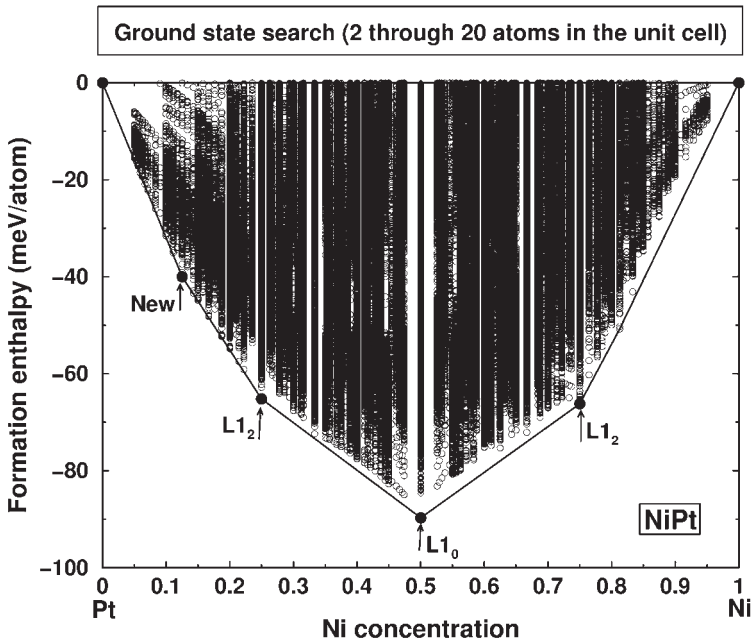

Figure 10. Ground state search for unit cells with up to 20 sites for Ni–Pt. Arrows denote the ground states identified out of 3 039 674 configurations.

These new ground states are at 33.3% and 60% Au concentration. The new structure at 33.3% is located 4.8 meV atom^{-1} below the tie line connecting the ground states at concentration 25% and 50%. We next calculated the energy of this structure using the *ab initio* LDA method. The calculated LDA energy (-47.7 meV atom^{-1}) was in good agreement with CE prediction energy (-46.1 meV atom^{-1}). Also we calculate the LDA energy of the new ground state at 60% Au concentration. The calculated energy value was -48.8 meV atom^{-1} which is in good agreement with the CE value of -48.9 meV atom^{-1}. When we include these new ground states in the input set of our CE, we find that our CE is stable with respect to addition of these new structures, i.e. we are finding the same ground state structures before and after addition of these two structures to the input set.

For Cu–Au, we use a cut-off energy of 80 meV so that any structure whose energy lies above the ground state line by more than this amount is discarded from the input set. If we include these high-energies structures, we could not get a good fit for low-energies structures. Figure 15 shows the elimination error plot for a fit including very high energy structures ($\Delta H = 32.5$, 52.2, 78.6 and 61.4 meV atom^{-1} for $L1_1$, $v2$ (A_3B_1 $\langle 111\rangle$), $v1$, (A_2B_2 $\langle 111\rangle$) and $\alpha 1$ (A_3B_1 $\langle 111\rangle$), respectively). We see large elimination errors even in low-energy structures, such as $\alpha 2$, $b1$ and $b2$ (A_1B_2 $\langle 111\rangle$, A_2B_1 $\langle 001\rangle$ and A_1B_2 $\langle 001\rangle$, respectively). However, excluding high-energy structures from the fit gives much lower elimination errors (see figure 15).

The ground state search (direct enumeration) using the CE for ScS–□S yielded 12 ground states for concentrations $0 < x \leqslant \frac{1}{3}$. The only experimentally known ground state for this system occurs at $x = \frac{1}{3}$. In the literature, this structure is known as Sc_2S_3 although a more appropriate nomenclature would be $Sc_2\,\square_1S_3$. This structure is a face-centred orthorhombic structure based on the underlying fcc lattice and has 12 scandium sites per primitive unit cell.

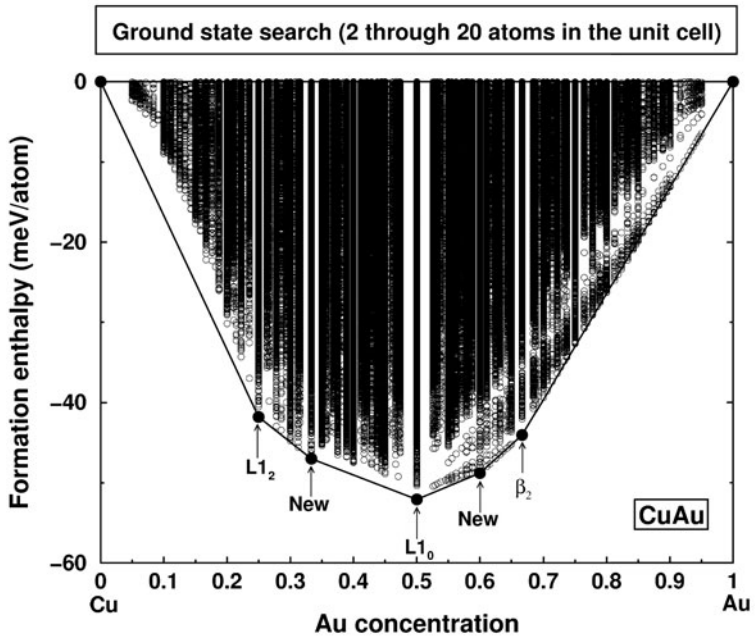

Figure 11. Ground state search for Cu–Au (see caption of figure 10).

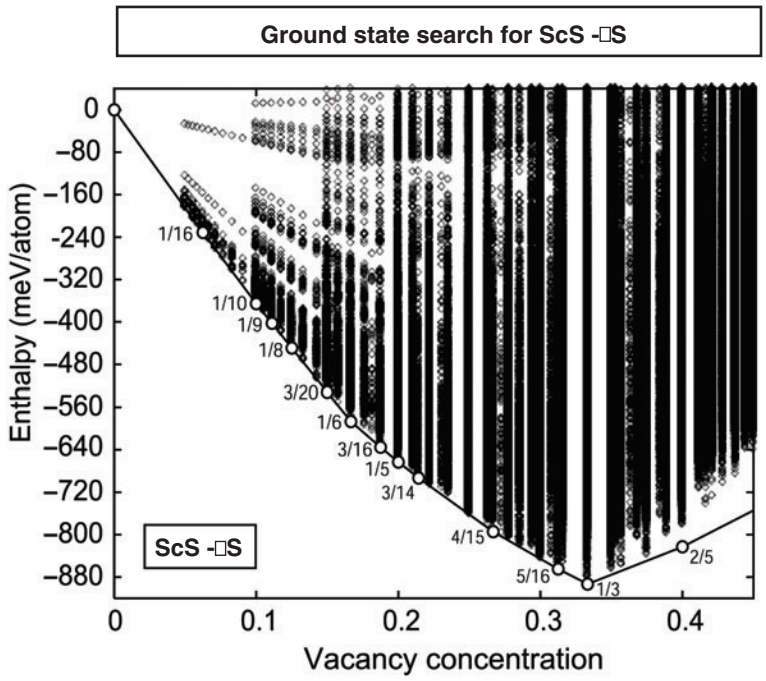

Figure 12. Ground state search for $Sc_{1-x}\,\square_x S$ (see caption of figure 10).

Table 1. New ground state predicted by the CE for Ni–Pt.

Structure	Lattice vectors	Atomic positions	$\boldsymbol{k}$-vectors
$NiPt_7$	1 0 0	Ni 0 0 0	$0\ 0\ \frac{1}{2}$
	0 1 0	Pt $\frac{1}{2}\ \frac{1}{2}$ 0	0 0 1
	$\frac{1}{2}\ \frac{1}{2}$ 2	Pt $\frac{1}{2}$ 1 $\frac{1}{2}$	$1\ 0\ \frac{1}{4}$
		Pt 1 $\frac{1}{2}\ \frac{1}{2}$	
		Pt 1 1 1	
		Pt $\frac{1}{2}\ \frac{1}{2}$ 1	
		Pt $\frac{1}{2}$ 1 $\frac{3}{2}$	
		Pt 1 $\frac{1}{2}\ \frac{3}{2}$	

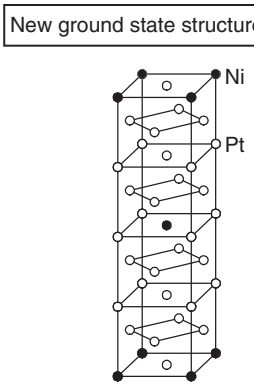

Figure 13. Crystal structure of the new ground state $NiPt_7$ predicted for Ni–Pt.

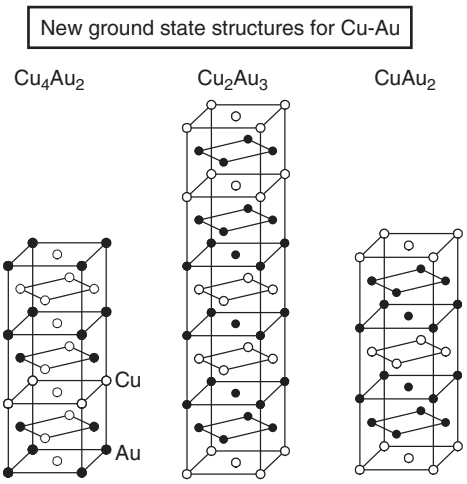

Figure 14. Crystal structures of the new ground states predicted for Cu–Au.

This structure is precisely that predicted by our CE at $x = \frac{1}{3}$. Experiments have hinted at the configuration of the ground states for $x < \frac{1}{3}$, but, to date, no definite results have been reported, though there are some striking similarities between CE-based Monte-Carlo simulations and the interpretation of x-ray data from some experimental studies. A complete exposition of

Table 2. New ground states predicted by the CE for Cu–Au.

Structure	Lattice vectors	Atomic positions	$\boldsymbol{k}$-vectors
Cu_4Au_2	1 0 0	Au 0 0 0	0 1 $\frac{1}{3}$
	0 1 0	Au 0 $\frac{1}{2}$ $\frac{1}{2}$	0 0 1
	0 $\frac{1}{2}$ $\frac{3}{2}$	Cu $\frac{1}{2}$ $\frac{1}{2}$ 0	
		Cu $\frac{1}{2}$ 1 $\frac{1}{2}$	
		Cu 0 1 1	
		Cu $\frac{1}{2}$ $\frac{1}{2}$ 1	
Cu_2Au_3	$\frac{1}{2}$ $\frac{1}{2}$ 0	Cu 0 0 0	0 0 1
	$\frac{1}{2}$ $-\frac{1}{2}$ 0	Cu $\frac{1}{2}$ 0 $-\frac{3}{2}$	0 0 $\frac{1}{2}$
	$\frac{1}{2}$ 0 $-\frac{5}{2}$	Au 1 0 -2	
		Au 1 0 -1	
		Au $\frac{1}{2}$ 0 $-\frac{1}{2}$	
$CuAu_2$ (β_2)	$\frac{1}{2}$ $\frac{1}{2}$ 0	Cu 0 0 0	0 0 1
	$-\frac{1}{2}$ $\frac{1}{2}$ 0	Au 0 $\frac{1}{2}$ $\frac{1}{2}$	
	0 $-\frac{1}{2}$ $\frac{3}{2}$	Au 0 0 1	

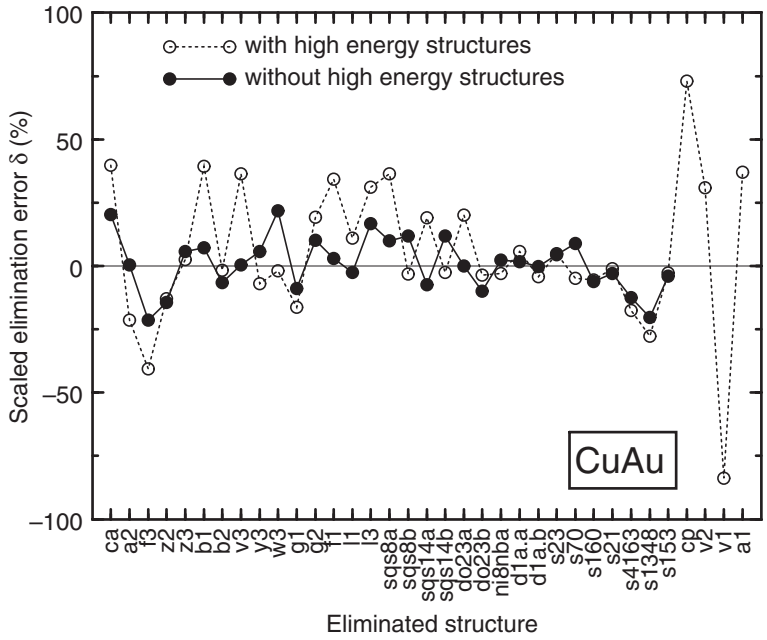

Figure 15. Elimination errors for Cu–Au with or without high-energy structures.

the ScS CE and its predictions, as well as references to the experimental studies, can be found in [51].

Figure 16 presents $J(\boldsymbol{k})$ for Ni–Pt and Cu–Au along the principal directions in the Brillouin zone. Since we have dealt with the singularity of $J_{\text{pair}}(\boldsymbol{k})$ at $k \to 0$ by separating the elastic strain energy of coherent superlattices in the long-period limit, we can see that $J_{\text{SR}}(k)$ has a finite value at $k \to 0$. Figure 17 presents the calculated pair interactions as a function of the near-neighbour fcc shell. We see that for Cu–Au, only the first five nearest-neighbour

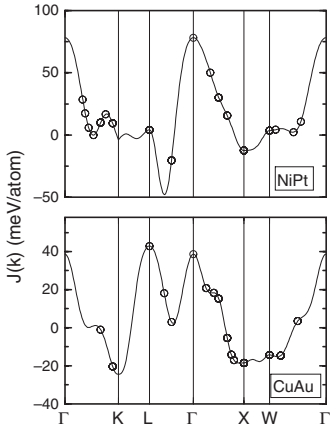

Figure 16. Fourier transform $J(\boldsymbol{k})$ of the pair interactions along the principal directions in the fcc Brillouin zone for Ni–Pt and Cu–Au.

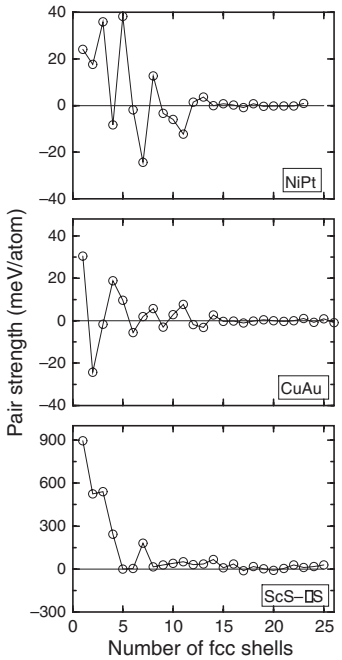

Figure 17. Pair interactions as a function of the near-neighbour fcc shell for Ni–Pt, Cu–Au and ScS–□S.

pair interactions are dominant, but in Ni–Pt the range is longer, with the third, fifth and seventh neighbour pair interactions are still very strong. Both Cu–Au and Ni–Pt have positive nearest-neighbour pair interactions which is consistent with the tendency towards complete miscibility and ordering at low temperatures. For ScS–□S only the first three pair interactions are dominant.

The multibody geometric figures included in the CE are defined in figure 18. The multibody energies are shown in figure 19. These figures illustrate the importance of the multibody terms in our Hamiltonian. We can see that dominant contributions are different

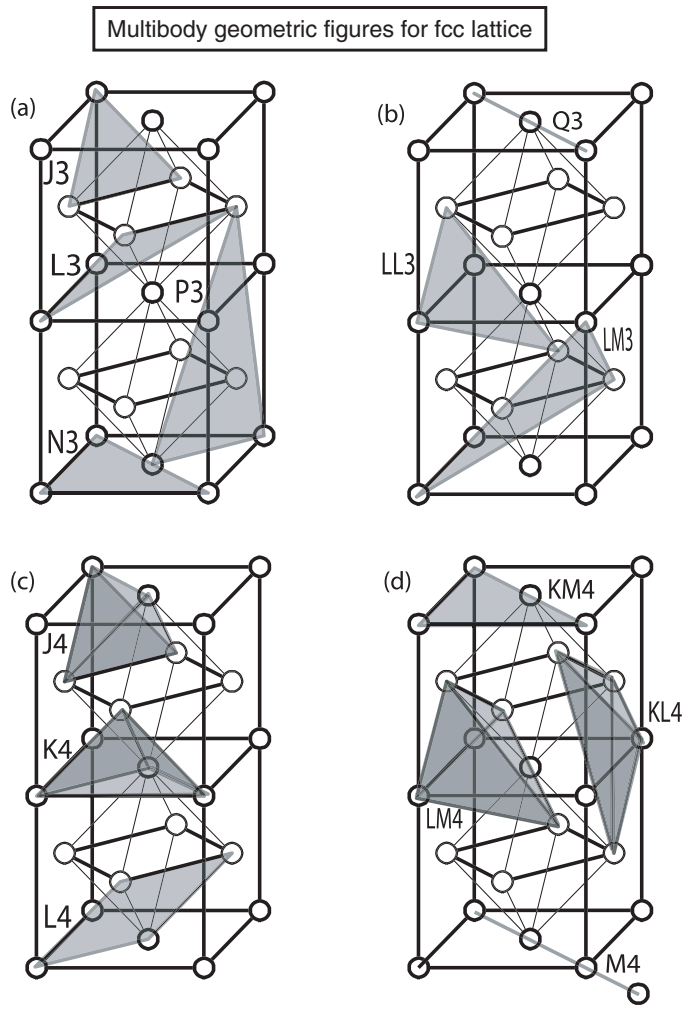

Figure 18. Multiatom geometric figures used in the CE.

for Cu–Au, Ni–Pt and ScS–□S. For Ni–Pt the empty site and three-body J_3 interactions are dominant, and the empty site, three-body J_3 and P_3 interactions are dominant for Cu–Au. However, for ScS–□S the single site term is the only dominant interaction.

6. Summary

The MBCE maps ≈20–40 LDA total energy calculations of rather simple binary A_pB_q compounds onto a generalized Ising expansion that includes an arbitrary number of pair and multibody interactions, as well as strain terms. This expansion predicts accurately the LDA energies of structures not included in the fit, and can hence be used, in conjunction with lattice statistical mechanics techniques to predict ground states, x-T phase diagrams, short-range order and alloy microstructures. An interesting aspect of this approach is that it can be used as an analytical tool to reveal the microscopic origins of thermodynamic behaviour. For example, one can use a set of model input energies that eliminate, on purpose, a specific

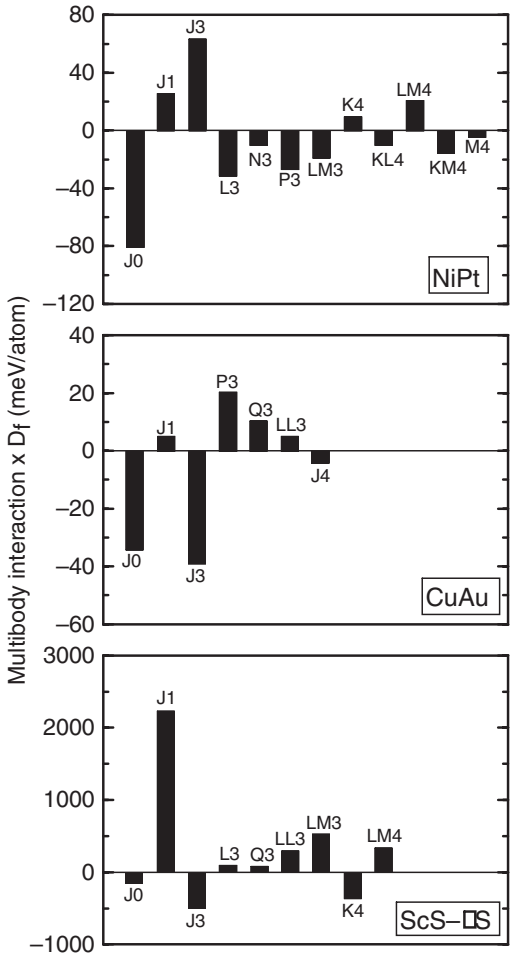

Figure 19. Multibody interaction energies for Ni–Pt, Cu–Au and ScS–□S (see figure 18 for the definition of the multibody terms).

bonding mechanism such as p–d coupling, or atomic relaxation, or relativistic correction, or spin-polarization, etc. Then using this set of energies one can generate the corresponding CE and predict the ensuing thermodynamic properties. By comparing these thermodynamic properties with those of the 'full' CE, one can shed light on the chemical bonding underpinning particular thermodynamic phenomena.

Acknowledgment

This work was supported by US DOE, office of Science, DMS, condensed-matter physics, under contract No DE-AC36-98-GO10337.

References

[1] Zunger A 1994 *Statics and Dynamics of Alloy Phase Transformations* vol 319, ed P E A Turchi and A Gonis (New York: Plenum) p 361

[2] de Fontaine D 1979 *Solid State Physics* vol 34, ed H Ehrenreich, F Seitz and D Turnbull (New York: Academic) p 73
[3] Kanamori J and Kakehashi Y 1977 *J. Physique* **38** 274
[4] Ducastelle F 1991 *Order and Phase Stability in Alloys* (Amsterdam: North-Holland)
[5] Ferreira L G, Wei S-H and Zunger A 1991 *Int. J. Supercomput. Appl.* **5** 34
[6] Binder K and Heerman D W 1988 *Monte Carlo Simulation in Statistical Physics* (Berlin: Springer)
[7] Polgreen T L 1984 *Phys. Rev.* B **29** 1468
[8] Wolverton C, Ozoliņš V and Zunger A 2000 *J. Phys.: Condens. Matter.* **12** 2749
[9] Schweika W and Haubold H-G 1988 *Phys. Rev.* B **37** 9240
[10] Müller S, Wang L-W, Zunger A and Wolverton C 1999 *Phys. Rev.* B **60** 16448
[11] Abrikosov I A, Vekilov Yu H and Ruban A V 1991 *Phys. Lett.* A **154** 407
[12] Car R and Parrinello M 1985 *Phys. Rev. Lett.* **55** 2471
[13] Payne M C, Teter M P, Allan D C, Arias T A and Joannopoulos J D 1992 *Rev. Mod. Phys.* **64** 1045
[14] Torrens I M 1972 *Interatomic Potentials* (New York: Academic)
Terakura K and Akai H 1992 *Interatomic Potentials and Structural Stability* (Berlin: Springer)
[15] Daw M S and Baskes M I 1984 *Phys. Rev.* B **29** 6443
[16] Domb C 1974 *Phase Transitions and Critical Phenomena* vol 3, ed C Domb and H S Green (London: Academica) p 358
[17] Styer D F, Phani M K and Lebowitz J L 1986 *Phys. Rev.* B **34** 3361
[18] Kikuchi R, Sanchez J M, de Fontaine D and Yamaguchi H 1980 *Acta Metall.* **28** 651
[19] Sigli C and Sanchez J M 1985 *Acta Metall.* **33** 1097
[20] Ferreira L G, Wei S-H and Zunger A 1989 *Phys. Rev.* B **40** 3197
[21] Wolverton C, Zunger A and Schönfeld B 1997 *Solid State Commun.* **101** 519
[22] Gyorffy B L and Stocks G M 1983 *Phys. Rev. Lett.* **50** 374
[23] Magri R, Wei S-H and Zunger A 1990 *Phys. Rev.* B **42** 11388
[24] Laks D B, Ferreira L G, Froyen S and Zunger A 1992 *Phys. Rev.* B **46** 12587
[25] Connolly J W D and Williams A R 1983 *Phys. Rev.* B **27** 5169
[26] Wolverton C, Ozoliņš V and Alex Zunger 1998 *Phys. Rev.* B **57** 4332
[27] Wei S-H, Mbaye A A, Ferreira L G and Zunger A 1987 *Phys. Rev.* B **36** 4163
[28] Ozoliņš V, Wolverton C and Zunger A 1998 *Phys. Rev.* B **57** 6427
[29] Lu Z W, Wei S-H and Zunger A 1991 *Phys. Rev. Lett.* **66** 1753
[30] Lu Z W, Wei S-H and Zunger A 1993 *Europhys. Lett.* **21** 221
[31] Wolverton C and Zunger A 1997 *Comput. Mater. Sci.* **8** 107
[32] Lu Z W, Klein B M and Zunger A 1995 *J. Phase Equilibria* **16** 36
[33] Lu Z W, Zunger A and Klein B M 1995 *J. Superlatt. Microstruct.* **18** 161
[34] Wolverton C, Zunger A and Lu Z W 1994 *Phys. Rev.* B **49** R10548
[35] Wolverton C and Zunger A 1995 *Phys. Rev.* B **52** 8813
[36] Lu Z W, Wei S-H and Zunger A 1992 *Phys. Rev. Lett.* **68** 1961
[37] Lu Z W, Wei S-H and Zunger A 1991 *Phys. Rev.* B **44** 10470
[38] Müller S and Zunger A 2001 *Phys. Rev. Lett.* **87** 165502
[39] Müller S, Wolverton C, Wang L W and Zunger A 2000 *Acta Materiala* **48** 4007
[40] Müller S and Zunger A 2001 *Phys. Rev.* B **63** 094204
[41] Osorio R and Froyen S 1993 *Phys. Rev.* B **47** 1889
[42] Wei S-H, Ferreira L G and Zunger A 1990 *Phys. Rev.* B **41** 8240
[43] Zunger A 1994 *Handbook of Crystal Growth* (Amsterdam: Elsevier) p 999
[44] Ozoliņš V, Wolverton C and Zunger A 1998 *Phys. Rev.* B **57** 4816
[45] Zunger A, Wei S-H, Ferreira L G and Bernard J E 1990 *Phys. Rev. Lett.* **65** 353
[46] Ceder G, Garbulsky G D and Tepesch P D 1995 *Phys. Rev.* B **51** 11257
[47] Froyen S 1989 *Phys. Rev.* B **39** 3168
[48] Garbulsky G D and Ceder G 1995 *Phys. Rev.* B **51** 67
[49] van de Walle A and Ceder G 2002 *J. Phase Equilibria* **23** 384
van de Walle A 2001 MIT Ab-initio Phase Stability (MAPS) code, http://www.mit.edu/˜avdw/maps/
[50] Sanati M, Wang L G and Zunger A 2002 *Phys. Rev. Lett.* submitted
[51] Hart G L W and Zunger A 2001 *Phys. Rev. Lett.* **87** 275508